Quantifying CineECG Output for Enhancing Electrocardiography Signals Classification

MHD Jafar Mortada, *Member, IEEE*, Agnese Sbrollini, *Member, IEEE*, Ilaria Marcantoni, *Member, IEEE*, Erica Iammarino, *Member, IEEE*, Laura Burattini, *Member, IEEE*, and Peter Van Dam

***Abstract*—CineECG, a vectorcardiography-based method, uses standard 12-lead electrocardiography and 3D heart and torso models to depict the electrical activation path during the heart cycle, offering detailed visualization of cardiac electrical activity without numerical quantification. Our research aims to quantify CineECG outputs by defining 54 features that describe the route, shape, and direction of electrical activation. These features were used to develop a multinomial regression model classifying electrocardiography signals into normal sinus rhythm, left bundle branch block, right bundle branch block, and undetermined abnormalities. Trained and tested on 6,860 signals from the PhysioNet/Computing in Cardiology Challenge 2020 and THEW project, the model achieved an F1 score over 84% (normal sinus rhythm: 93%, left bundle branch block: 93%, right bundle branch block: 90%, undetermined abnormalities: 84%). The results suggest CineECG's potential in enhancing electrocardiography interpretation and aiding in the accurate diagnosis of various abnormalities.**

***Index Terms*—CineECG, electrocardiography, left bundle branch block, right bundle branch block, vectorcardiography.**

***Impact Statement*—Utilizing quantified CineECG output, achieved 89.68% global accuracy in classifying ECG signals, thus enhancing ECG interpretation and aiding in the accurate diagnosis of cardiac abnormalities.**

Received 18 February 2025; revised 17 April 2025 and 26 June 2025; accepted 27 June 2025. Date of publication 10 July 2025; date of current version 30 July 2025. This work was supported in part by PNRR, Mission 4, Component 2 through Research to the Company - Investment 3. 3, in part by the Introduction of Innovative Doctoral Programs through the Innovative Needs of Companies and Promote the Recruitment of Researchers from Companies, under Grant DM 117/2023 and Grant 39-033-01-DOT1301942-8805. The review of this article was arranged by Editor Riccardo Barbieri. *(Corresponding author: Laura Burattini.)*

MHD Jafar Mortada is with the Department of Information Engineering, Università Politecnica delle Marche, 60131 Ancona, Italy, and also with PEACS BV, 6845 Arnhem, The Netherlands.

Agnese Sbrollini, Ilaria Marcantoni, Erica Iammarino, and Laura Burattini are with the Department of Information Engineering, Università Politecnica delle Marche, 60131 Ancona, Italy (e-mail: l.burattini@univpm.it).

Peter Van Dam is with the Center for Digital Medicine and Robotics, Jagiellonian University Medical College, 30-688 Kraków, Poland, and also with PEACS BV, 6845 Arnhem, The Netherlands.

Digital Object Identifier 10.1109/OJEMB.2025.3587993

I. Introduction

THE electrocardiogram (ECG) is a fundamental diagnostic non-invasive and low-cost tool in cardiology, providing valuable insights into cardiac electrical activity. Since its standardization into 12-leads ECG by the American Heart Association in 1954 [1] it is the most used test in the daily clinical routine, considering its ability to capture the electrical activity of the heart from multiple angles [2]. Any modification from the standard waveform can be an index of dysfunction or pathology [3]; thus, an accurate ECG interpretation is mandatory for early detection and management of heart conditions (e.g., arrhythmia), or to guide treatment decisions (e.g., medication) and interventions (e.g., ablation). Moreover, regular ECG monitoring may help to track disease progression, improve patient outcomes and prevent misdiagnosis, reducing risks of inappropriate treatments or delayed actions.

Standard 12-lead ECG is widely used to diagnose cardiac abnormalities. However, ECG interpretation is still a very challenging task due to intersubject variability (e.g., differences in heart anatomy, electrical conduction patterns … etc.), intrasubject variability (stress, artifacts, medication … etc.) and symptoms similarities, (e.g., left bundle branch block (LBBB; Fig. 1(b)) and right bundle branch block (RBBB; Fig. 1(c)) are common conduction abnormalities marked by prolonged QRS duration compared to that of a healthy subject with normal sinus rhythm (NSR; Fig. 1(a))). However, in LBBB, the electrical pathway to the left ventricle is compromised, specifically in the His-Purkinje system, provoking a delay in the depolarization [4], [5] On the contrary, RBBB is caused by a compromission of the electrical pathway to the right ventricle [6]. Moreover, the cardiac electrical pathway is not recognizable from the 12-leads. These issues make the visual ECG interpretation and classification hard (accuracy is estimated to be around 54% [7]).

In the literature, vectorcardiography (VCG) was proposed as a different representation of the cardiac electrical activity to simultaneously obtain both spatial and temporal information. VCG assumes that the source of cardiac electrical activity is a single fixed dipole, represented as a fixed origin vector in 3D space (body anatomical axis). VCG can be estimated from the standard 12-lead ECG using a 3-by-8 matrix of coefficients [8]. Despite its potential as spatial-temporal representation of the electrical heart activity, VCG is difficult to interpret because of its complex patterns. Moreover, VCG is susceptible to

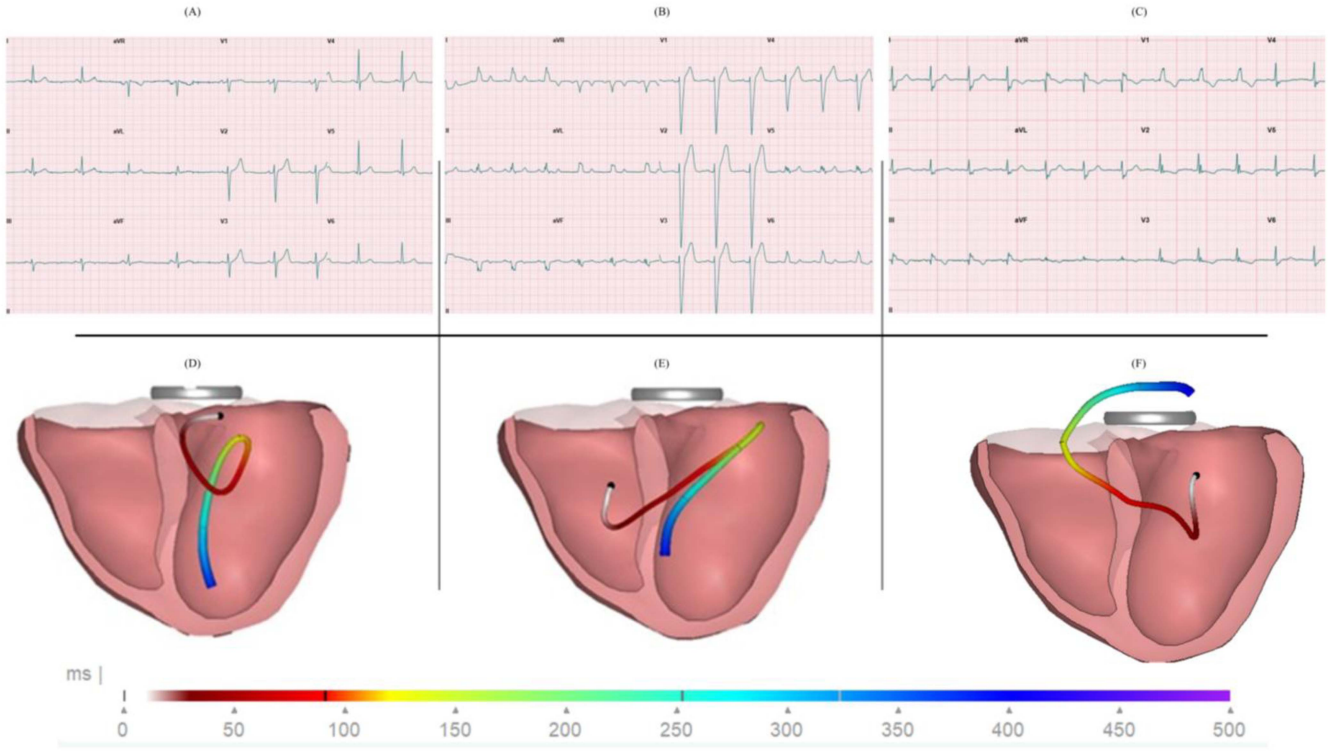

Fig. 1. Standard 12-lead ECG, (a) for an NSR case, (b) for a case diagnosed with LBBB, and (c) for a case diagnosed with RBBB and PathECG generated by CineECG for (d). NSR case, (e), LBBB case, and (f), RBBB case, the time map is represented as a colored line at the bottom of the figure. In the standard ECG of an LBBB patient we can observe a prolonged QRS duration, with broad notched or slurred R waves in leads I, aVL, V5, and V6, an RS pattern in leads V5 and V6 due to displaced QRS transition; absence of Q waves in leads I, V5, and V6; a narrow Q wave in lead aVL without myocardial pathology; R-peak time longer than 60ms in leads V5; and ST and T waves in the opposite direction to the QRS complex. In the standard ECG of an LBBB patient, a prolonged QRS duration can be noticed as well, while in leads V1 or V2 an rsr′, rsR′, rSR′, or rarely a qR pattern is observed, with the R′ or r′ deflection typically wider than the initial R wave ;some patients may show a wide, often notched R wave pattern in leads V1 and/or V2. Additionally, an S wave longer than the R wave or exceeding 40ms in leads I and V6 is noted in adults. The R peak time is normal in leads V5 and V6 but exceeds 50ms in lead V1. While in PathECG, NSR, propagates through the septum, moves toward the apex and the left free wall, before making a turn towards the base at around R peak occurrence, propagates towards the apex while shifting to the interior and the septum, and finally moves toward the apex during the T-wave. In LBBB, PathECG starts from the right ventricle, travels through the septum to the left ventricle, and during the repolarization, travels from the left ventricle to the right ventricle. Finally, in RBBB PathECG starts from the left ventricle, moves towards the right ventricle through the septum, and then upon the repolarization travels toward the base.

information loss, because of the simple assumption it relies on (i.e., fixed dipole).

Another spatial-temporal representation of the heart electrical activity, named CineECG [9], was introduced. CineECG provides PathECG, an easy-to-interpret view of the cardiac electrical activity by combining the standard 12-lead ECG with the 3D heart and torso models. PathECG represents the average anatomical location of the cardiac cells that simultaneously undergo a change in transmembrane potential at a certain point of time. It overcomes the main limitation of VCG by using the heart axis as the frame of reference of a moving vector. Panel D of Fig. 1 shows PathECG of a healthy subject, showing normal sinus rhythm (NSR), while panels E and F show PathECG of patients affected by LBBB and RBBB respectively. PathECG is very intuitive because it is visually associated with the physiopathology of heart depolarization and repolarization. Moreover, PathECG is mapped into an anatomical model of the patient's heart, allowing for a personalized interpretation and avoiding issues related to inter- subject variability, typical of traditional ECG. Several studies demonstrated the utility of CineECG as visual tool in the clinical setting [10], [11]. Differently, Pociask et al. [12] attempted a quantitative approach by evaluating the percentage of PathECG and median ECG waves (termed WaveECG) falling within normal trends (Fig. 2) obtained using 14380 standard 12-lead ECG recordings taken from the Physikalisch Technische Bundesanstalt (PTB-XL) database, achieving an accuracy of 87%. However, this approach used only one feature (percentage) to interpret PathECG and WaveECG and provided only normal/abnormal classification.

The aim of the present work is to quantify PathECG and WaveECG with multiple features and to investigate the importance of these features in discriminating NSR, LBBB, RBBB and other cardiac rhythms.

II. Materials and Methods

A. Data

Overall, 6860 standard 12-lead ECG were used in this study- The ECGs categorized into four classes: 2645 NSR, 635 LBBB, 1580 RBBB, and 2000 undetermined (UND, i.e.,

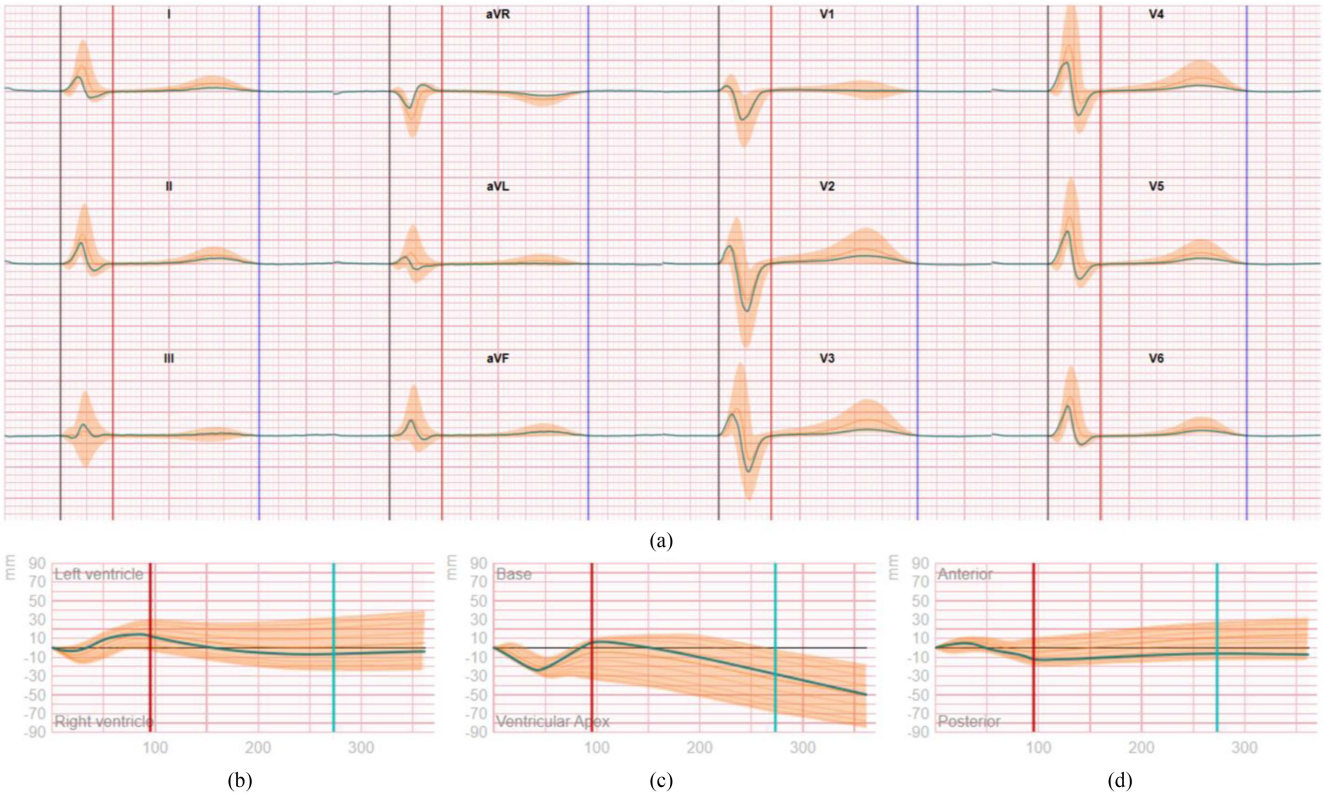

Fig. 2. (a) WaveECG for the standard 12-lead ECG. (b)–(d) 2D projections of PathECG normal trends across three cardiac anatomical planes: (b) Left–right, (c) base–apex, and (d) anterior–posterior. The shaded orange areas represent the normal signal trends. An example signal (shown in green) falling within the range is provided to illustrate a healthy case. Vertical lines mark key points: black, red and blue for QRS onset, offset and T-wave offsets respectively in WaveECG, and red and green for QRS offset and T-wave onset in PathECG.

cases presenting diagnosis of other ventricular disorders). These ECGs were taken from two dataset sources: 6425 ECGs (3375 M, 3050 F, 56.89±17.68 Years) were taken from The PhysioNet/Computing in Cardiology Challenge 2020 [13], which includes: the CPSC/CPSC-Extra Database, containing 10330 12-lead ECG stored for the "China Physiological Signal Challenge" in 2018 [14] (records last from 6s to 60s; sampled at 500 Hz); the St Petersburg INCART 12-lead Arrhythmia Database, containing 74 recordings derived from 32 Holter monitor records (records last 30 minutes; sampled at 257 Hz); and the Georgia database, containing 10344 12-lead ECGs (records lasts 10s; sampled at 500 Hz). Annotation related to encoded diagnosis was available for each record. 435 ECGs (284 M, 151 F, Age not available) were taken from the "Strict LBBB" from The Telemetric and Holter ECG Warehouse (THEW) hosted by University of Rochester Medical Center [15]. It included 10s 12-lead Mason-Likar ECGs, taken from 602 patients (sampled at 1 kHz). To ensure data homogeneity, ECGs with double diagnoses were not included. Signals that are distorted by noise in a way that it is not possible to detect key points to computing WaveECG were not included as well. When considering the THEW dataset, only ECGs annotated as "Strict LBBB" and "LBBB" were included [16]. To simulate a real clinical scenario, the UND category was created, by considering data acquired from subjects presenting diagnosis of ventricular disorders.

B. CineECG Methodology

CineECG algorithm [9] requires three inputs (Fig. 3(a)), the 12-lead ECG, and the heart and the torso 3D models (if not available, like in this study generic models are used). Initially, ECG baseline correction is performed, and the WaveECG is computed (Fig. 3(b)). Then, VCG is calculated by using a recursive approach (Fig. 3(c)) detailed in (1):

$$\overrightarrow{\mathrm{VCG(t)}} = \sum_{\mathrm{n}=1}^{9} \mathrm{L_n(t)}\ \mathrm{a_n} \left(\frac{\tilde{\mathrm{r}}_\mathrm{n} - \tilde{\mathrm{r}}_\mathrm{ref}(\mathrm{t})}{||\tilde{\mathrm{r}}_\mathrm{n} - \tilde{\mathrm{r}}_\mathrm{ref}(\mathrm{t})||} \right) \tag{1}$$

where: $\overrightarrow{\mathrm{VCG(t)}}$ is the VCG vector at a certain point of time t; $\mathrm{L_n}$ is the ECG of the lead number n (n =1 …9, representing the 3 fundamental leads and the 6 precordial leads respectively); $\mathrm{a_n}$ is a scaling factor; $\tilde{\mathrm{r}}_\mathrm{n}$ is a vector from center of mass of the heart (assumed to be the reference point) to the nth lead electrode (provided by the 3D models); eventually, $\tilde{\mathrm{r}}_\mathrm{ref}(\mathrm{t})$ is either the CineECG vector at $(\mathrm{t}-1)$ (defined as in (2)), or 0 if at time origin $(\mathrm{t}=0)$, set in correspondence of mid QRS-complex occurrence. Finally, VCG is used to calculate CineECG vector (Fig. 3(d)) as in (2):

$$\overrightarrow{\mathrm{CineECG}\,(\mathrm{t})} = \overrightarrow{\mathrm{CineECG}\,(\mathrm{t}-1)} + \mathrm{velocity} \frac{\overrightarrow{\mathrm{VCG}}}{||\overrightarrow{\mathrm{VCG}}||} \tag{2}$$

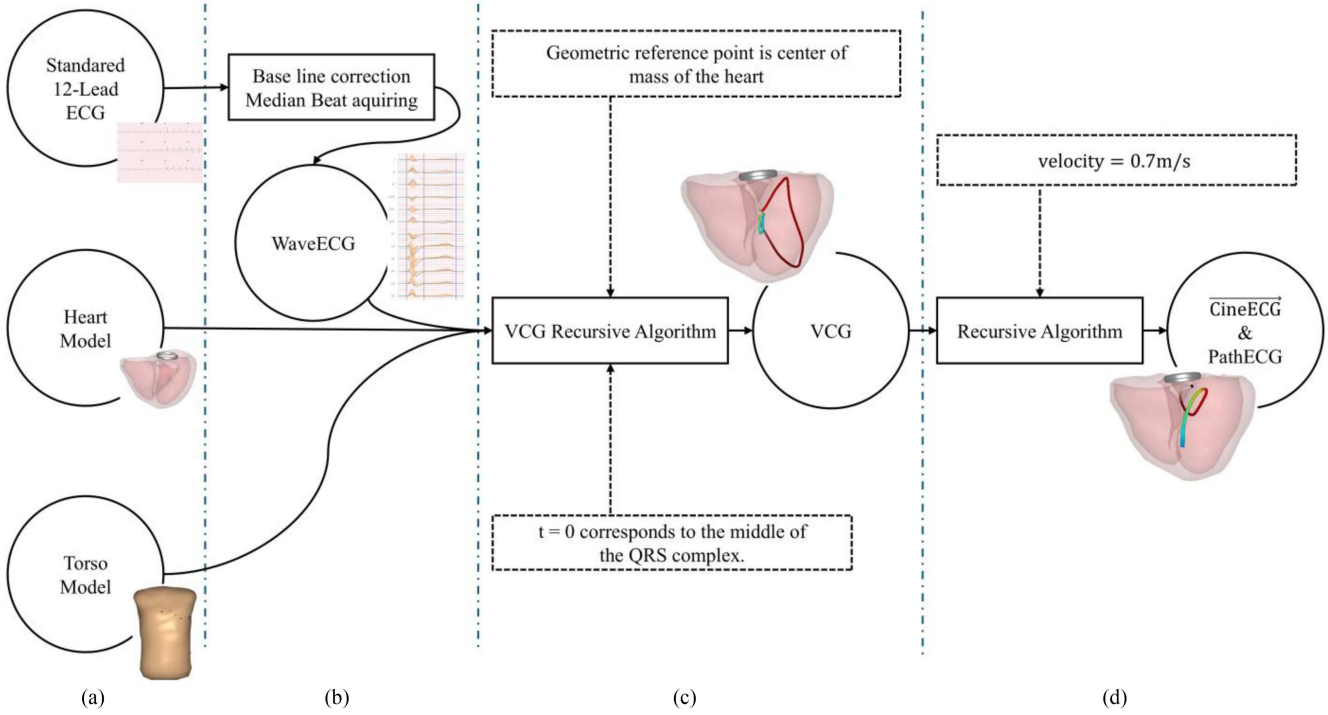

Fig. 3. Flowchart representing the CineECG algorithm, starting with input gathering (panel A), WaveECG computation (panel B), VCG vector calculation (panel C) and CineECG victor calculation, from which PathECG is obtained (panel D). Circles represent input/output, solid rectangles represent processes, and dashed rectangles and arrows represent assumptions.

where velocity represents the step speed at which a new CineECG vector is computed and is assumed to be 0.7 m/s. This assumption is a tradeoff between the longitudinal propagation speed of the action potential, its transmural propagation speed and its speed in areas with a dense concentration of Purkinje-myocardial junctions [9]. The calculation is performed forward in time (t>0) and backward in time (t<0) to cover the WaveECG segment from QRS-complex onset to T-wave end. The path of $\overrightarrow{\mathrm{CineECG(t)}}$ in the heart model is PathECG.

C. Feature Extraction

CineECG features consist of the 54 features reported and described in Table I. They were used to quantify CineECG output, i.e., WaveECG and PathECG. Physiologically, CineECG features allow for a detailed interpretation of ECG morphologies, capturing different segments of ventricular depolarization and repolarization. Indeed, WaveECG contains information about ECG amplitude and shape, while PathECG contains information about ECG shape and direction of the action potential propagation. Deviations of WaveECG and PathECG from those of healthy subjects, which are considered as references, reflect abnormalities in the cardiac electrical.

D. Classification Model Construction

A classification model was constructed to classify the data into four classes, which are NSR, LBBB, RBBB and UND. The data were split into train and test sets, using 50% as a splitting ratio [17]. The training set was used to train a model, while the test set was used only to evaluate the model performance to avoid overfitting. Since this is a multiclass problem, a multinomial logistic regression (MLR) was utilized. MLR is an extension of the binary logistic regression, allowing the possibility to model the probabilities of possible outcome of a categorical dependent variable. Each outcome (in this study there are four classes, thus k = 1, 2, 3, 4 and K = 4) is associated with a probability $P(Y = k)$, where the probability of an outcome is computed as in (3):

$$\mathrm{P\,(Y = kx)} = \frac{\exp\left(\beta_{0\mathrm{k}} + \mathrm{x} \cdot \beta_{\mathrm{k}}\right)}{\sum_{\mathrm{j}=1}^{\mathrm{K}} \exp\left(\beta_{0\mathrm{j}} + \mathrm{x} \cdot \beta_{\mathrm{j}}\right)} \tag{3}$$

where Y is the outcome, x is the vector of input features, β_{k} is the vector of coefficients for outcome *k* and $\beta_{0\mathrm{k}}$ is the intercept for outcome *k*. The model was implemented inside a Python environment, trained using Newton-Raphson method based on the conjugate gradient algorithm as optimization algorithm.

E. Statistical Analysis

To evaluate the performance of the proposed model, the receiver operating characteristic (ROC) using one-vs-all analysis were computed and characterized in terms of area under the curve (AUC) and 95% confidence intervals (95%CI). For each class we evaluated the confusion matrix, considering the 50% operating point, and the following evaluation metrics: the accuracy (ACC), positive predictive value (PPV), negative predictive values (NPV), false discovery rate (FDR), false omission rate (FOR), true positive rate(TPR), false negative rate (FNR), false positive rate(FPR), true negative rate (TNR), Matthews correlation coefficient (MCC), and F1 score (F1), in both training

TABLE I
CINEECG FEATURES ACRONYMS AND DESCRIPTION

#	Acronym	Description
1	σ_P	StD of the difference between PathECG and reference PathECG along QRS.
2	$\sigma_{P^{ST}}$	StD of the difference between PathECG and reference PathECG along ST and T
3	σ_W	StD of the difference between WaveECG and reference WaveECG along QRS
4	$\sigma_{W^{STT}}$	StD of the difference between WaveECG and reference WaveECG along ST and T
5	TCR_{89}	TCR at 89ms: 3D distance between points at 0ms and 89ms points divided by QRS width
6	TCR	TCR: 3D distance between start and end points of PathECG divided by QRS width
7	TCR_{QRS}	TCR of QRS: 3D distance between start and end points of PathECG QRS divided by QRS width
8	TCR_{ST}	TCR of ST: 3D distance between start and end of PathECG ST divided by QRS width
9	$TCR_{60\%QRS}$	TCR of 60%QRS: 3D distance between start and 60% of PathECG QRS divided by QRS width
10	$\%P$	% of PathECG within healthy trend
11	$\%P_{ST}$	% of PathECG corresponding to ST within reference PathECG trend
12	$\%P_{STT}$	% of PathECG corresponding to ST and T wave within reference PathECG trend
13	$\%P_T$	% of PathECG T wave within reference PathECG trend
14	$\%P_{0-29}$	% of PathECG in the first 29ms within reference PathECG trend
15	$\%P_{0-89}$	% of PathECG in the first 89ms within reference PathECG trend
16	$\%P_{0-110}$	% of PathECG in the first 110ms within reference PathECG trend
17	$\%P_{30-59}$	% of PathECG ranging between 30ms and 59ms within reference PathECG trend
18	$\%P_{60-89}$	% of PathECG ranging between 60ms and 89ms within reference PathECG trend
19	$\%P_{90-129}$	% of PathECG ranging between 90ms and 129ms within reference PathECG trend
20	$\%P_{90-169}$	% of PathECG ranging between 90ms and 169ms within reference PathECG trend
21	$\%P_{110-200}$	% of PathECG ranging between 110ms and 200ms within reference PathECG trend
22	$\%P_{130-169}$	% of PathECG ranging between 130ms and 169ms within reference PathECG trend
23	$\%P_{170-Tp}$	% of PathECG ranging between 170ms and T peak within reference PathECG trend
24	$\%P_{200-Tp}$	% of PathECG ranging between 200ms and T peak within reference PathECG trend
25	%W	% of WaveECG within reference WaveECG trend
26	$\%W_{ST}$	% of WaveECG ST within reference WaveECG trend
27	$\%W_{STT}$	% of WaveECG ST and T wave within reference WaveECG trend
28	$\%W_T$	% of WaveECG T wave within reference WaveECG trend
29	$\%W_{0-29}$	% of WaveECG in the first 29ms within reference WaveECG trend
30	$\%W_{0-89}$	% of WaveECG in the first 89ms within reference WaveECG trend
31	$\%W_{0-110}$	% of WaveECG in the first 110ms within reference WaveECG trend
32	$\%W_{30-59}$	% of WaveECG ranging between 30ms and 59ms within reference WaveECG trend
33	$\%W_{60-89}$	% of WaveECG ranging between 60ms and 89ms within reference WaveECG trend
34	$\%W_{90-129}$	% of WaveECG ranging between 90ms and 129ms within reference WaveECG trend
35	$\%W_{90-169}$	% of WaveECG ranging between 90ms and 169ms within reference WaveECG trend
36	$\%W_{110-200}$	% of WaveECG ranging between 110ms and 200ms within reference WaveECG trend
37	$\%W_{130-169}$	% of WaveECG ranging between 130ms and 169ms within reference WaveECG trend
38	$\%W_{170-Tpeak}$	% of WaveECG ranging between 170ms and T peak within reference WaveECG trend
39	$\%W_{200-Tpeak}$	% of WaveECG ranging between 200ms and T peak within reference WaveECG trend
40	$\%QRS_L$	% of the PathECG QRS directed toward the left direction
41	$\%End_L$	% of PathECG of the last 25ms of QRS directed toward the left direction
42	$\%Range_L$	% of PathECG ranging between 110ms and 150ms directed toward the left direction
43	$\%QRS_A$	% of PathECG QRS directed toward the anterior direction
44	$\%End_A$	% of PathECG of the last 25ms of QRS directed toward the anterior direction
45	$\%Range_A$	% of PathECG ranging between 110ms and 150ms directed toward the anterior direction
46	$\%QRS_B$	% of PathECG QRS directed toward the base direction
47	$\%End_B$	% of PathECG of the last 25ms of QRS directed toward the base direction
48	$\%Range_B$	% of PathECG ranging between 110ms and 150ms directed toward the base direction
49	QRS_{AB}	Length of Apex-Base projection of PathECG QRS averaged direction
50	$Range_{AB}$	Length of Apex-Base projection of PathECG averaged direction ranging between 110ms and 150ms
51	QRS_{PA}	Length of Posterior-Anterior projection of PathECG QRS averaged direction
52	$Range_{PA}$	Length of Posterior-Anterior projection of PathECG averaged direction ranging between 110ms and 150ms
53	QRS_{RL}	Length of Right-Left projection of PathECG QRS averaged direction
54	$Range_{RL}$	Length of Right-Left projection of PathECG averaged direction ranging between 110ms and 150ms

StD: Standard Deviation, TCR: Trans Cardiac Ratio. Reference PathECG/WaveECG trend: is the set of PathECG/WaveECG of the healthy subjects in [13]; refernce PathECG/WaveECG is the median of the reference PathECG/WaveECG trend.

and testing sets:

$$ACC = {TP + TN}/{TN + TP + FP + FN} \quad (4)$$

$$\text{PPV} = {\text{TP}}/{\text{TP} + \text{FP}} \quad (5)$$

$$\text{NPV} = {\text{TN}}/{\text{PN}} \quad (6)$$

$$\text{FDR} = {\text{FP}}/{\text{TP} + \text{FP}} \quad (7)$$

$$\text{FOR} = {\text{TN}}/{\text{PN}} \quad (8)$$

$$\text{TPR} = {\text{TP}}/{\text{TP} + \text{FN}} \quad (9)$$

$$\text{FNR} = {\text{FN}}/{\text{TP} + \text{FN}} \quad (10)$$

$$\text{FPR} = {\text{FP}}/{\text{TP} + \text{FN}} \quad (11)$$

$$\text{TNR} = {\text{TN}}/{\text{TN} + \text{FP}} \quad (12)$$

$$\text{MCC} = \sqrt{\text{TPR} \times \text{TNR} \times \text{PPV} \times \text{NPV}} - \sqrt{\text{FNR} \times \text{FPR} \times \text{FOR} \times \text{FDR}} \quad (13)$$

$$\text{F1} = {}^{2 \times \text{PPV} \times \text{TPR}}/_{\text{PPV} + \text{TPR}} \quad (14)$$

where TP are the true positives, TN are the true negatives, FP are the false positives, FN are the false negatives. Additionally, Global Accuracy (GACC) was computed as the proportion of correctly classified cases out of the total number of cases across all classes. To evaluate the role of each feature in the assignment of a specific class, the values of the coefficients associated to each feature assigned to each class were ranked: by magnitude indicates the strength of the relationship, while the sign reflects the effect in the response variable. Moreover, the Wald Test was applied to the coefficient to test the hypothesis of the coefficient equal to zero (significance level set at 0.05). Finally, artificial neural networks (ANN) consist of one hidden layer, support vector machine (SVM), decision tree (DT) and random forest (RF) were implemented to compare the method with other machine learning methods.

III. Results

Panel A of Fig. 4 presents violin plots showing the distribution of all 54 extracted features across the four classification categories, and panels B through E display the ROC curves for each class, along with the corresponding AUC values and 95%CI. Evaluation metrics for each class and model, across both training and test sets, are summarized in Table II. For the ANN, SVM, DT, and RF models, the relative performance difference compared to the MLR model is also reported. The MLR model achieved a GACC of 91.14% on the training set and 89.68% on the test set. Table III lists the coefficient values of the MLR model for each class. Notably, 85% (46 out of 54) of the CineECG features were statistically significant (i.e., coefficients significantly different from zero) in at least one class, highlighting the relevance of these features for classification. Fig. 5 illustrates a bar chart of the actual coefficient values, annotated with feature ranks. The ranks are presented in descending order of coefficient magnitude, where rank 1 corresponds to the feature with the highest absolute coefficient value, and rank 55 to the lowest (among the features we considered the intercept as well).

IV. Discussion

This study quantified PathECG and WaveECG with multiple features and investigated the importance of these features in discriminating NSR, LBBB, RBBB and UND. CineECG Features (Table I) were selected to capture key aspects of WaveECG and PathECG deviations. Such deviations were characterized in terms of their magnitude (quantified by the WaveECG and PathECG percentage within reference trends) their location (indicated by the analyzed ECG segments) and their nature (quantified by the TCR and direction). Results indicate that these features were able to distinguish between normal and abnormal patterns while ensuring interpretability. Alternative features such as frequency-domain coefficients were considered in unreported preliminary evaluations, but were successively excluded due to redundancy, or difficulty of interpretability. Given the large amount of data, 50%/50% split was used [17] where 50% of the data was kept hidden from the training procedure to ensure the generalization of the model and to prevent it from overfitting and was used to measure the performance of the model. Evaluation metrics demonstrated that the model performs well across all classes, with particularly high TPR (95.31%, 92.45%) for the NSR and LBBB classes, indicating strong classification performance for these rhythms. The balanced TPR and PPV values for the UND class also indicate reliable performance for more ambiguous cases. High TNR values indicate that the model is very effective at identifying negative cases for each class, with almost perfect TNR for LBBB, while the high TOR values, especially for SNR, indicate that the model is highly effective at identifying positive cases, with a drop for UND. The Wald test showed that only a few features (15%) were not statistically significant for classification; however, most (85%) of the features were statistically significant in at least one class. The importance of the features was evaluated using the magnitude of their coefficients. Some similarities were found among classes (Fig. 5); for example, both NSR and UND share σ_W as the highest amplitude while RBBB and LBBB share $\%Range_L$These findings agree with what we see in panels D and E in Fig. 2 as PathECG, in both cases, is diverted from the normal path by going toward the left ventricle in case of LBBB (hence the positive sign of the coefficient), and toward the right ventricle in case of RBBB (hence the negative sign of the coefficient) because of their compromised electrical path. In fact, this difference in the sign of the coefficients between the two classes appeared in multiple features especially if related to left/right direction, which is an agreement with what is known in clinics. Across classes, the coefficients related to direction showed higher amplitudes compared to those related to the portion of both PathECG and WaveECG inside the normal trend and those related to TCR. This might be due to the chosen cardiac abnormalities (LBBB, RBBB).

We use MLR model based on its interpretability, but we also compared other models. SVM, DT and RF did not show improvement in terms of the evaluation metrics, specifically in the test where these models showed overfitting.

Differently, ANN showed some improvements, due to its ability to better handle non-linearity, while this confirms the efficiency of deep learning techniques [18], ANN nature makes clinical interpretation hard and requires more resources than other models. In some cases, ANN even requires a graphic processing unit to train, that also means higher training time, unlike MLR, which has linear complexity, thus its training time is lower and can be interpreted using its coefficients.

In previous research, CineECG was used to study complex conduction disorders and showed a high ability to describe complex cases. Examples are the evaluation of group beating bradycardia with a combination of RBBB and left anterior fascicular Wenckebach block, along with a Mobitz II block in the left posterior fascicle [19], the evaluation of a case of Brugada syndrome, which is a life-threatening genetic disorder affecting the heart rhythm (arrhythmia) [20], and familial ST-segment depression syndrome [11]. Furthermore, CineECG

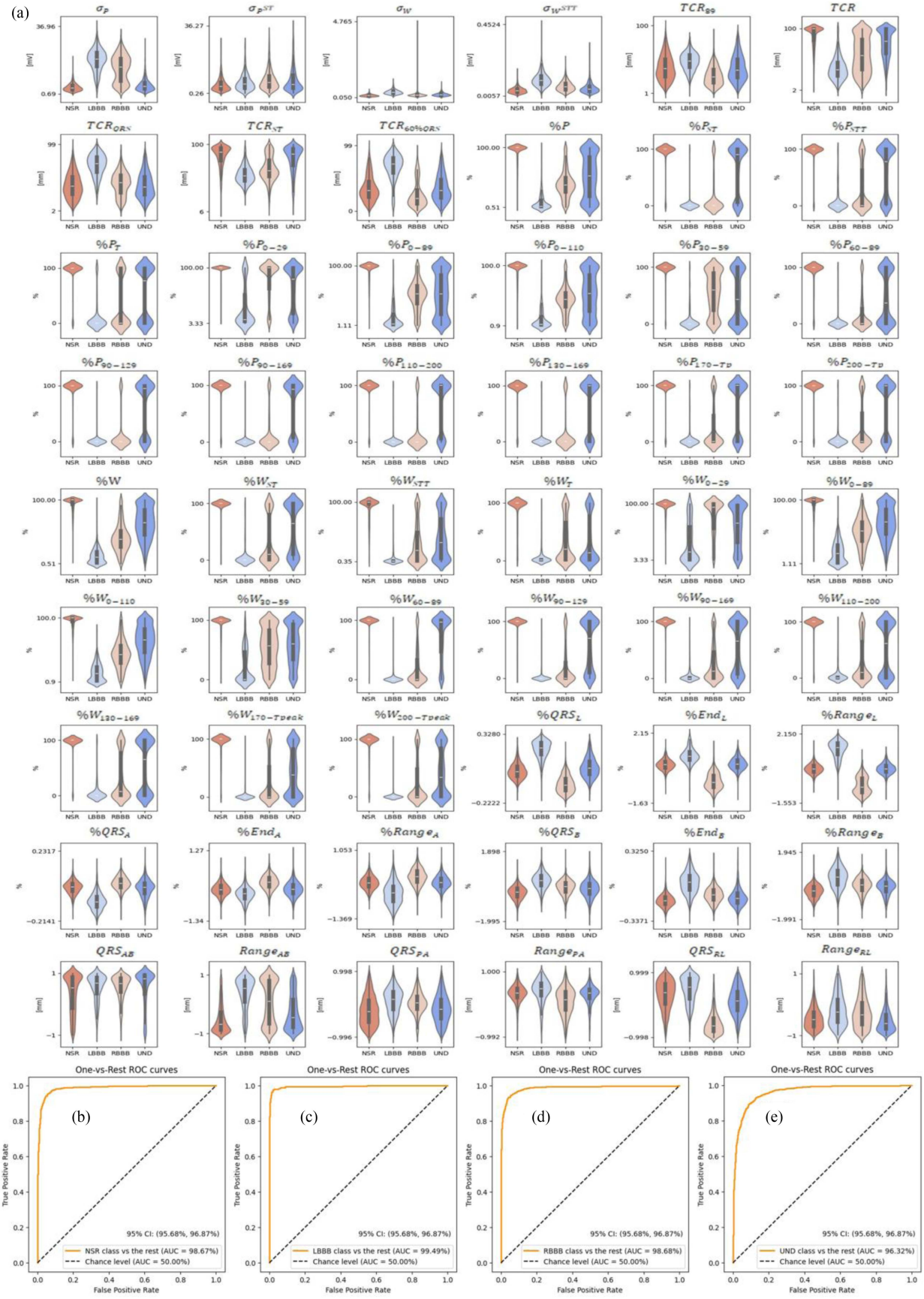

Fig. 4. Feature distributions and classification performance. (a) Violin plots depicting the distribution of all 54 extracted features across the four classification categories. (b)–(e) receiver Operating Characteristic (ROC) curves for each class, illustrating the model's performance. Area under the curve (AUC) values and corresponding 95% confidence intervals (CI) are shown for each ROC curve.

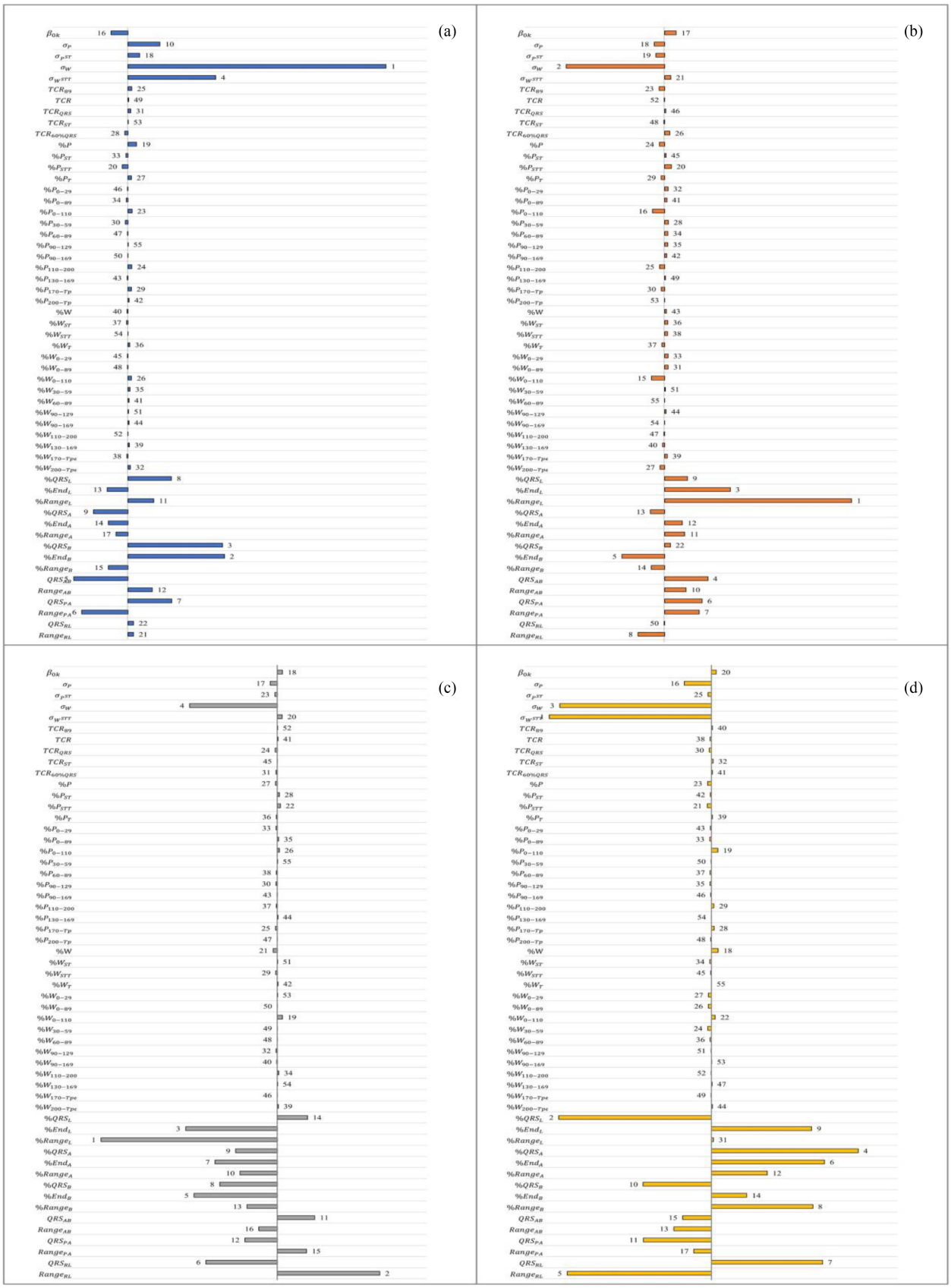

Fig. 5. Bar graph displaying the values of the model coefficients, with each bar labeled by a number indicating the descending order of the coefficient's amplitude for each class displaying the performance for each class: NSR (panel a), LBBB (panel b), RBBB (panel c), and UND (panel d).

TABLE II
EVALUATION METRICS FOR EACH CLASS (SNR, LBBB, RBBB, UND) AND MODEL (MLR, ANN, SVM, DT, RF) IN BOTH TRAINING AND TEST

			TP	TN	FP	FN	ACC (%)	PPV (%)	NPV (%)	FDR (%)	FOR (%)	TPR (%)	FNR (%)	FPR (%)	TNR (%)	MCC (%)	F1 (%)	GACC (%)
TRAINING	MLR	SNR	1263	2008	100	59	95	93	97	7	3	96	4	5	95	90	94	91
		LBBB	294	3096	16	24	99	95	99	5	1	92	8	1	99	93	94	
		RBBB	704	2586	54	86	96	93	97	7	3	89	11	2	98	88	91	
		UND	865	2296	14	135	92	87	94	13	6	87	14	6	94	81	87	
	ANN	SNR	1320^{+57}	2073^{+65}	31^{-69}	6^{-53}	99^{+4}	98^{+5}	100^{+3}	2^{-5}	0^{-3}	100^{+4}	0^{-4}	1^{-4}	99^{+4}	98^{+8}	99^{+5}	99^{+8}
		LBBB	294^{0}	3136^{+40}	0^{-16}	0^{-24}	100^{+1}	100^{+5}	100^{+1}	0^{-5}	0^{-1}	100^{+8}	0^{-8}	0^{-1}	100^{+1}	100^{+7}	100^{+6}	
		RBBB	790^{+86}	2627^{+41}	5^{-49}	8^{-78}	$100+^{4}$	99^{+6}	100^{+3}	1^{-6}	0^{-3}	99^{+10}	1^{-10}	0^{-2}	100^{+2}	99^{+11}	99^{+8}	
		UND	982^{+117}	2410^{+114}	8^{-126}	30^{-105}	99^{+7}	99^{+12}	99^{+5}	1^{-12}	1^{-5}	97^{+10}	3^{-11}	0^{-6}	100^{+6}	97^{+16}	98^{+11}	
	SVM	SNR	1287^{+24}	2021^{+13}	83^{-17}	39^{-20}	96^{+1}	94^{+1}	98^{+1}	6^{-1}	2^{-1}	97^{+1}	3^{-1}	4^{-1}	96^{+1}	93^{+3}	95^{+1}	94^{+3}
		LBBB	279^{-15}	3131^{+35}	5^{-11}	15^{-9}	99^{0}	98^{+3}	100^{+1}	2^{-3}	0^{-1}	95^{+3}	5^{-3}	0^{-1}	100^{+1}	96^{+3}	97^{+3}	
		RBBB	734^{+30}	2600^{+14}	32^{-22}	64^{-22}	97^{+1}	96^{+3}	98^{+1}	4^{-3}	2^{-1}	92^{+3}	8^{-3}	1^{-1}	99^{+1}	92^{+4}	94^{+3}	
		UND	915^{+50}	2323^{+27}	95^{-39}	97^{-38}	94^{+2}	91^{+4}	96^{+2}	9^{-4}	4^{-2}	90^{+3}	10^{-4}	4^{-2}	96^{+2}	87^{+6}	91^{+4}	
	DT	SNR	1326^{+63}	2104^{+96}	0^{-100}	0^{-59}	100^{+5}	100^{+7}	100^{+3}	0^{-7}	0^{-3}	100^{+4}	0^{-4}	0^{-5}	100^{+5}	100^{+10}	100^{+6}	100^{+9}
		LBBB	294^{0}	3136^{+40}	0^{-16}	0^{-24}	100^{+1}	100^{+5}	100^{+1}	0^{-5}	0^{-1}	100^{+8}	0^{-8}	0^{-1}	100^{+1}	100^{+7}	100^{+6}	
		RBBB	798^{+94}	2632^{+46}	0^{-54}	0^{-86}	100^{+4}	100^{+7}	100^{+3}	0^{-7}	0^{-3}	100^{+11}	0^{-11}	0^{-2}	100^{+2}	100^{+12}	100^{+9}	
		UND	1012^{+147}	2418^{+122}	0^{-134}	0^{-135}	100^{+8}	100^{+13}	100^{+6}	0^{-13}	0^{-6}	100^{+13}	0^{-14}	0^{-6}	100^{+6}	100^{+19}	100^{+13}	
	RF	SNR	1326^{+63}	2104^{+96}	0^{-100}	0^{-59}	100^{+5}	100^{+7}	100^{+3}	0^{-7}	0^{-3}	100^{+4}	0^{-4}	0^{-5}	100^{+5}	100^{+10}	100+6	100^{+9}
		LBBB	294^{0}	3136^{+40}	0^{-16}	0^{-24}	100^{+1}	100^{+5}	100^{+1}	0^{-5}	0^{-1}	100^{+8}	0^{-8}	0^{-1}	100^{+1}	100^{+7}	100+6	
		RBBB	798^{+94}	2632^{+46}	0^{-54}	0^{-86}	100^{+4}	100^{+7}	100^{+3}	0^{-7}	0^{-3}	100^{+11}	0^{-11}	0^{-2}	100^{+2}	100^{+12}	100+9	
		UND	1012^{+147}	2418^{+122}	0^{-134}	0^{-135}	100^{+8}	100^{+13}	100^{+6}	0^{-13}	0^{-6}	100^{+13}	0^{-14}	0^{-6}	100^{+6}	100^{+19}	100+13	
TEST	MLR	SNR	1261	1977	130	62	94	91	97	9	3	95	5	6	94	88	93	90
		LBBB	293	3093	20	24	99	94	99	6	1	92	8	1	99	92	93	
		RBBB	701	2571	69	89	95	91	97	9	3	89	11	3	97	87	90	
		UND	821	2295	135	179	91	86	93	14	7	82	18	6	94	78	84	
	ANN	SNR	1259^{-2}	2038^{+61}	73^{-57}	60^{-2}	96^{+2}	95^{+4}	97^{0}	5^{-4}	3^{0}	95^{0}	5^{0}	3^{-3}	97^{+3}	92^{+4}	95^{+2}	91^{+1}
		LBBB	316^{+23}	3066^{-27}	23^{+3}	25^{+1}	99^{0}	93^{-1}	99^{0}	7^{+1}	1^{0}	93^{+1}	7^{-1}	1^{0}	99^{0}	92^{0}	93^{0}	
		RBBB	697^{-4}	2567^{-4}	81^{+12}	85^{-4}	95^{0}	90^{-1}	97^{0}	10^{+1}	3^{0}	89^{0}	11^{0}	3^{0}	97^{0}	86^{-1}	89^{-1}	
		UND	846^{+25}	2307^{+12}	135^{0}	142^{-37}	92^{+1}	86^{0}	94^{+1}	14^{0}	6^{-1}	86^{+4}	14^{-4}	6^{0}	94^{0}	80^{+2}	86^{+2}	
	SVM	SNR	1255^{-6}	2028^{+51}	83^{-47}	64^{+2}	96^{+2}	94^{+3}	97^{0}	6^{-3}	3^{0}	95^{0}	5^{0}	4^{-2}	96^{+2}	91^{+3}	94^{+1}	90^{0}
		LBBB	314^{+21}	3072^{-21}	17^{-3}	27^{+3}	99^{0}	95^{+1}	99^{0}	5^{-1}	1^{0}	92^{0}	8^{0}	1^{0}	99^{0}	93^{+1}	93^{0}	
		RBBB	680^{-21}	2591^{+20}	57^{-12}	102^{+13}	95^{0}	92^{+1}	96^{-1}	8^{-1}	4^{+1}	87^{-2}	13^{+2}	2^{-1}	98^{+1}	87^{0}	90^{0}	
		UND	855^{+34}	2273^{-22}	169^{+34}	133^{-46}	91^{0}	83^{-3}	94^{+1}	17^{+3}	6^{-1}	87^{+5}	13^{-5}	7^{+1}	93^{-1}	79^{+1}	85^{+1}	
	DT	SNR	1137^{-124}	1965^{-12}	146^{+16}	182^{+120}	90^{-4}	89^{-2}	92^{-5}	11^{+2}	8^{+5}	86^{-9}	14^{+9}	7^{+1}	93^{-1}	80^{-8}	87^{-6}	84^{-6}
		LBBB	312^{+19}	3049^{-44}	40^{+20}	29^{+5}	98^{-1}	89^{-5}	99^{0}	11^{+5}	1^{0}	91^{-1}	9^{+1}	1^{0}	99^{0}	89^{-3}	90^{-3}	
		RBBB	668^{-33}	2535^{-36}	113^{+44}	114^{+25}	93^{-2}	86^{-5}	96^{-1}	14^{+5}	4^{+1}	85^{-4}	15^{+4}	4^{+1}	96^{-1}	81^{-6}	85^{-5}	
		UND	754^{-67}	2182^{-113}	260^{+125}	234^{+55}	86^{-5}	74^{-12}	90^{-3}	26^{+12}	10^{+3}	76^{-6}	24^{+6}	11^{+5}	89^{-5}	65^{-13}	75^{-9}	
	RF	SNR	526^{-735}	1267^{-710}	844^{+714}	793^{+731}	52^{-42}	38^{-53}	62^{-35}	62^{+53}	38^{+35}	40^{-55}	60^{+55}	40^{+34}	60^{-34}	0^{-88}	39^{-54}	30^{-60}
		LBBB	20^{-273}	2825^{-268}	264^{+244}	321^{+297}	83^{-16}	7^{-87}	90^{-9}	93^{+87}	10^{+9}	6^{-86}	94^{+86}	9^{+8}	91^{-8}	-3^{-95}	6^{-87}	
		RBBB	173^{-528}	2055^{-516}	593^{+524}	609^{+520}	65^{-30}	23^{-68}	77^{-20}	77^{+68}	23^{+20}	22^{-67}	78^{+67}	22^{+19}	78^{-19}	0^{-87}	22^{-68}	
		UND	296^{-525}	1728^{-567}	714^{+579}	692^{+513}	59^{-32}	29^{-57}	71^{-22}	71^{+57}	29^{+22}	30^{-52}	70^{+52}	29^{+23}	71^{-23}	1^{-77}	30^{-54}	

The relative difference between the performance of a model and mlr performance are reported in apex.

showed promising results in visualizing the changes in the electrical activity in ischemic patients [10]. Despite these results, none of these works tried to provide an automatic diagnostic tool by quantifying the paths generated by CineECG. Boonstra et al. [21] tried to quantify the output of CineECG to train a model and perform classification into five classes, by applying the quantification approach based on calculating the mean temporo-spatial isochrone trajectory. The research considered only 500 patients, which was not sufficient to statistically cover all the class variances. Differently, our work tried to overcome the shortage of data by including multiple data sources (from publicly available databases), guaranteeing also reproducibility of the results. Moreover, our work investigated many features that are derived from the CineECG output. The approach of characterizing the paths into features provides a better understanding of the algorithm and its output, moving the interpretation from being visual to quantitative numerical. Clinically this method would provide a useful clinical tool that would combine the visual heart anatomical-based output (PathECG), that is easier to interpret than the traditional 12-lead ECG, with a categorical diagnosis, and since CineECG is a user-friendly tool, it can be integrated into real life clinical scenarios, as a cloud service for emergency environments like ambulances, or as stand-alone software on workstations in hospitals and clinics. Indeed, CineECG can deal

TABLE III
VALUES OF EACH MODEL COEFFICIENT FOR EACH CLASS

	NSR	LBBB	RBBB	UND
β_{0k}	-0.2283	0.1218	0.0670	0.0396
σ_P	0.4274*	-0.1124	-0.0976*	-0.2175*
$\sigma_P{}^{ST}$	0.1544*	-0.0938*	-0.0342*	-0.0264
σ_W	3.4531	-1.0558*	-1.1774	-1.2199*
$\sigma_W{}^{STT}$	1.1743*	0.0644	0.0637*	-1.3024*
TCR_{B9}	0.0502*	-0.0600*	0.0009	0.0089
TCR	0.0080	-0.0068	0.0084*	-0.0096*
TCR_{QRS}	0.0363*	0.0117	-0.0301	-0.0179
TCR_{ST}	0.0012	-0.0103	-0.0053*	0.0144*
$TCR_{60\%QRS}$	-0.0436*	0.0547	-0.0200	0.0089
$\%P$	0.1138*	-0.0576	-0.0260*	-0.0302*
$\%P_{ST}$	-0.0300*	0.0133	0.0256*	-0.0089*
$\%P_{STT}$	-0.0776	0.0703	0.0404	-0.0331*
$\%P_T$	0.0446*	-0.0384*	-0.0154	0.0093
$\%P_{0-29}$	-0.0092*	0.0355*	-0.0178	-0.0086
$\%P_{0-89}$	-0.0260	0.0231*	0.0159	-0.0131
$\%P_{0-110}$	0.0528	-0.1310	0.0263	0.0518
$\%P_{30-59}$	-0.0368*	0.0399	0.0001*	-0.0032*
$\%P_{60-89}$	-0.0087	0.0329*	-0.0139	-0.0104
$\%P_{90-129}$	0.0001*	0.0324	-0.0210*	-0.0116
$\%P_{90-169}$	-0.0069	0.0205	-0.0074	-0.0062
$\%P_{110-200}$	0.0503*	-0.0552	-0.0148*	0.0197
$\%P_{130-169}$	-0.0139	0.0086	0.0061	-0.0008
$\%P_{170-Tp}$	0.0428*	-0.0377	-0.0266	0.0215
$\%P_{200-Tp}$	0.0147	-0.0052	-0.0048	-0.0048*
$\%W$	-0.0158	0.0188	-0.0577*	0.0547*
$\%W_{ST}$	-0.0208	0.0319	0.0018	-0.0128*
$\%W_{STT}$	-0.0009	0.0297	-0.0226*	-0.0062
$\%W_T$	0.0231*	-0.0310*	0.0078	0.0000*
$\%W_{0-29}$	-0.0110*	0.0346	0.0005	-0.0241*
$\%W_{0-89}$	-0.0086*	0.0363	-0.0020	-0.0257*
$\%W_{0-110}$	0.0466	-0.1426*	0.0651*	0.0309
$\%W_{30-59}$	0.0255*	0.0070	-0.0033	-0.0292*
$\%W_{60-89}$	0.0148*	-0.0009	-0.0034	-0.0105
$\%W_{90-129}$	0.0067	0.0141	-0.0185*	-0.0023*
$\%W_{90-169}$	0.0119*	-0.0048*	-0.0090	0.0019*
$\%W_{110-200}$	-0.0044	-0.0108*	0.0174	-0.0022
$\%W_{130-169}$	0.0172*	-0.0237*	0.0004	0.0061
$\%W_{170-Tpeak}$	-0.0175	0.0266	-0.0051	-0.0040
$\%W_{200-Tpeak}$	0.0302	-0.0503*	0.0122	0.0079
$\%QRS_L$	0.5813*	0.2433	0.4024	-1.2271*
$\%End_L$	-0.2803*	0.7032	-1.2289	0.8060*
$\%Range_L$	0.3435	2.0017*	-2.3618*	0.0166
$\%QRS_A$	-0.4650*	-0.1550	-0.5607	1.1807*
$\%End_A$	-0.2633	0.1893	-0.8357*	0.9096
$\%Range_A$	-0.1616	0.2142	-0.5024	0.4498
$\%QRS_B$	1.2636*	0.0600*	-0.7742	-0.5494
$\%End_B$	1.2921*	-0.4589*	-1.1176*	0.2845*
$\%Range_B$	-0.2631	-0.1449	-0.4076	0.8157
QRS_{AB}	-0.7295	0.4623	0.4986	-0.2315
$Range_{AB}$	0.3239	0.2289	-0.2497	-0.3031
QRS_{PA}	0.5842	0.4011	-0.4371*	-0.5482
$Range_{PA}$	-0.6205*	0.3706	0.3910*	-0.1411
QRS_{RL}	0.0731*	-0.0082	-0.9588*	0.8940
$Range_{RL}$	0.0742	-0.2861*	1.3715*	-1.1596*

*P-value <0.05

with signals coming from different machines without requiring any preprocessing; thus, this tool potentially represents a fast diagnostic tool that combines specific diagnostic with visual output in support clinical decision Despite its strengths, CineECG presents the limitation of using generic torso and heart models, whose can affect the calculation of the VCG. However, the interpretation of the CineECG path may be more personalized if the software would be combined with an auto segmentation of the heart and torso from imaging modalities. Thus, future studies will evaluate the possibility of evaluating the possible integration of image processing tools in CineECG, to have a complete personalized tool, but the main limitations of this study are related to the availability of annotated ECG data and comparison with the experience of clinicians. Indeed, some disease categories have a limited availability of ECG (e.g., LBBB), and others are not available (e.g., acute coronary syndrome). Moreover, a quantitative comparison with clinical experience should be assessed to demonstrate if our machine learning tool interpretation may support clinical practice. Therefore, future works can investigate the possibility to include data from more abnormalities and to validate the classification through manual visual inspection of clinical experts across a different population.

IV. CONCLUSION

CineECG can be characterized in terms of quantitative features that can be used as inputs for an efficient heart-rhythm classification model. CineECG features provides a better understanding of the CineECG algorithm and of its outputs (PathECG and WaveECG), moving the interpretation from being only visual to also quantitative.

CONFLICT OF INTEREST

Peter Van Dam is an owner of Peacs BV and ECG Excellence BV, which are in the process of commercializing the CineECG algorithms. MHD Jafar Mortada has a scholarship co-funded by Peacs BV. The remaining authors declare no potential conflicts of interest.

AUTHOR CONTRIBUTIONS

MHD Jafar Mortada: Conceptualization, Methodology, Software, Validation, Formal analysis, investigation, Data Curation, Writing original draft, Writing review and editing. Agnese Sbrollini: Methodology, Validation, Formal analysis, Writing review and editing. Ilaria Marcantoni: Writing review and editing, Visualization. Erica Iammarino: Data Curation, Writing review and editing, Visualization. Laura Burattini: Validation, Formal analysis, Resources, Writing review and editing, Supervision, Project administration, Funding acquisition. Peter Van Dam: Conceptualization, Software, Writing review and editing, Supervision, Project administration, Funding acquisition.

REFERENCES

[1] F. N. Wilson et al., "Recommendations for standardization of electrocardiographic and vectorcardiographic leads," *Circulation*, vol. 10, no. 4, pp. 564–573, 1954, doi: 10.1161/01.CIR.10.4.564.

[2] R. Klabunde, *Cardiovascular Physiology Concepts*. Philadelphia, PA, USA: Lippincott Williams & Wilkins, 2011.
[3] A. L. Goldberger, Z. D. Goldberger, and A. Shvilkin, *Goldberger's Clinical Electrocardiography: A Simplified Approach*, 10th ed.. Amsterdam, The Netherlands: Elsevier, 2023.
[4] N. Y. Tan, C. M. Witt, J. K. Oh, and Y.-M. Cha, "Left bundle branch block: Current and future perspectives," *Circulation Arrhythmia Electrophysiol.*, vol. 13, no. 4, Apr. 2020, Art. no. e008239, doi: 10.1161/CIRCEP.119.008239.
[5] F. M. Kusumoto et al., "2018 ACC/AHA/HRS guideline on the evaluation and management of patients with bradycardia and cardiac conduction delay: A report of the American college of cardiology/American heart association task force on clinical practice guidelines and the heart rhythm society," *Circulation*, vol. 140, no. 8, pp. e382–e482, 2019, doi: 10.1161/CIR.0000000000000628.
[6] T. Ikeda, "Right bundle branch block: Current considerations," *Curr. Cardiol. Rev.*, vol. 17, no. 1, pp. 24–30, 2021.
[7] D. A. Cook, S.-Y. Oh, and M. V. Pusic, "Accuracy of physicians' electrocardiogram interpretations: A systematic review and meta-analysis," *JAMA Intern. Med.*, vol. 180, no. 11, pp. 1461–1471, Nov. 2020, doi: 10.1001/jamainternmed.2020.3989.
[8] J. A. Kors, G. Van Herpen, A. C. Sittig, and J. H. Van Bemmel, "Reconstruction of the frank vectorcardiogram from standard electrocardiographic leads: Diagnostic comparison of different methods," *Eur. Heart J.*, vol. 11, no. 12, pp. 1083–1092, Dec. 1990, doi: 10.1093/oxfordjournals.eurheartj.a059647.
[9] M. J. Boonstra, D. H. Brooks, P. Loh, and P. M. van Dam, "CineECG: A novel method to image the average activation sequence in the heart from the 12-lead ECG," *Comput. Biol. Med.*, vol. 141, 2022, Art. no. 105128.
[10] I. van der Schaaf, M. Kloosterman, A. P. M. Gorgels, P. Loh, and P. M. van Dam, "CineECG for visualization of changes in ventricular electrical activity during ischemia," *J. Electrocardiol.*, vol. 83, pp. 50–55, 2024.
[11] R. Frosted et al., "CineECG analysis provides new insights into familial ST-segment depression syndrome," *Europace*, vol. 25, no. 5, 2023, Art. no. euad116.
[12] E. Pociask, K. P. Malinowski, M. H. D. J. Mortada, K. K. Proniewska, and P. M. van Dam, "Automatic classification normal ECGs based on normal PathECG and WaveECG features," in *Proc. 2023 Comput. Cardiol.*, 2023, pp. 1–4.
[13] E. A. P. Alday et al., "Classification of 12-lead ECG: The physIoNet/computing in cardiology challenge 2020," *Physiol. Meas.*, vol. 41, no. 12, 2020, Art. no. 124003.
[14] F. Liu et al., "An open access database for evaluating the algorithms of electrocardiogram rhythm and morphology abnormality detection," *J. Med. Imag. Health Inform.*, vol. 8, no. 7, pp. 1368–1373, 2018.
[15] J.-P. Couderc, "The telemetric and holter ECG warehouse initiative (THEW): A data repository for the design, implementation and validation of ECG-related technologies," in *Proc. 2010 Annu. Int. Conf. IEEE Eng. Med. Biol.*, 2010, pp. 6252–6255.
[16] D. G. Strauss, R. H. Selvester, and G. S. Wagner, "Defining left bundle branch block in the era of cardiac resynchronization therapy," *Amer. J. Cardiol.*, vol. 107, no. 6, pp. 927–934, 2011, doi: 10.1016/j.amjcard.2010.11.010.
[17] V. R. Joseph, "Optimal ratio for data splitting," *Stat. Anal. Data Mining: ASA Data Sci. J.*, vol. 15, no. 4, pp. 531–538, Apr. 2022, doi: 10.1002/sam.11583.
[18] Y. Ansari, O. Mourad, K. Qaraqe, and E. Serpedin, "Deep learning for ECG arrhythmia detection and classification: An overview of progress for period 2017–2023," *Front. Media*, vol. 14, 2023, Art. no. 1246746, doi: 10.3389/fphys.2023.1246746.
[19] I. van der Schaaf, M. Kloosterman, M. J. Boonstra, P. M. van Dam, and A. P. M. Gorgels, "CineECG illustrating the ventricular activation sequence in progressive AV-junctional conduction block," *J. Electrocardiol.*, vol. 78, pp. 1–4, 2023.
[20] P. M. van Dam et al., "Novel CineECG derived from standard 12-lead ECG enables right ventricle outflow tract localization of electrical substrate in patients with Brugada syndrome," *Circulation Arrhythmia Electrophysiol.*, vol. 13, no. 9, Sep. 2020, Art. no. e008524, doi: 10.1161/CIRCEP.120.008524.
[21] M. J. Boonstra, B. N. Hilderink, E. T. Locati, F. W. Asselbergs, P. Loh, and P. M. Van Dam, "Novel CineECG enables anatomical 3D localization and classification of bundle branch blocks," *EP Europace*, vol. 23, no. 1, pp. i80–i87, 2021.